Double Cantilever Indirect Tension Testing for Fracture of Quasibrittle Materials

Ferhun C. Caner*

Universitat Politècnica de Catalunya,
Institute of Energy Technologies and Dept. of Materials Science and Metallurgy,
Av. Eduard Maristany 16, 08019 Barcelona, Spain

A. Abdullah Dönmez

İstanbul Teknik Üniversitesi,
Department of Civil Engineering,
Ayazağa Kampüsü, 34469 Maslak/İstanbul, Turkey

Sıddık Şener

İstanbul Bilgi Üniversitesi,
Department of Civil Engineering,
santralistanbul Kampüsü, 34060 Eyüp/İstanbul, Turkey

Varol Koç

Ondokuz Mayıs Üniversitesi,
Department of Civil Engineering,
55139 Atakum/Samsun, Turkey

Abstract

The Double Cantilever Beam (DCB) Mode I fracture testing has been widely used in fracture testing of especially fiber reinforced polymer composites and adhesive joints. Application of classical DCB testing to plain concrete or

---

*Corresponding author

Email addresses: `ferhun.caner@upc.edu` (Ferhun C. Caner),
`donmezab@itu.edu.tr` (A. Abdullah Dönmez), `siddik.sener@bilgi.edu.tr` (Sıddık
Şener), `kvarol@omu.edu.tr` (Varol Koç)

unreinforced ceramic specimens is not straightforward and cannot be carried out as in fiber reinforced polymer composites. Instead, an indirect tension approach is proposed in this study. Tests of notched geometrically similar DCB specimens made of normal and high strength concretes loaded eccentrically at the cantilever beam-column ends in compression have been carried out. Classical type II size effect analyses of peak loads obtained from these tests are performed. The Microplane Model M7 is calibrated independently using uniaxial compression tests and employed to predict the peak loads of both tested and virtual geometrically similar DCB specimens. The same size effect analyses are performed on the predicted peak loads and the errors in the fracture parameters of the classical size effect analysis are determined.

Keywords: Fracture mechanics, double cantilever beam specimen, size effect, Microplane Model M7, concrete

1. Introduction

Since 1967 when Hoagland [1] proposed a double cantilever beam (DCB) specimen to evaluate the plane strain fracture toughness of metals and showed that the critical stress intensity factor is dependent on the specimen geometry and the material properties of the metal by comparing the results to those obtained by other experimental methods, the DCB Mode I fracture testing has been applied extensively to polymer fiber composites and adhesive joints, and to a lesser extent, to other materials such as wood and metals. DCB Mode I fracture specimens have also been extensively analyzed by analytical,

2

semianalytical and numerical methods in the literature. Earlier applications of DCB Mode I fracture testing and analysis include DCB tests of Heady [2] used to measure the critical stress intensity factor for slow crack growth due to corrosion in high strength steels. The analyses of Kanninen [3, 4] involving a beam free in part and supported in part by an elastic foundation matched the experimental results only for initial crack extensions. Later studies employed a higher order plate theory that included transverse shear deformation [5] and Timoshenko beam supported on an elastic foundation [6, 7, 8, 9, 10, 11, 12]. The calculation of energy release rate in the DCB specimens made of fiber reinforced polymer composites loaded in direct Mode I fracture has been widely studied [13, 14, 15, 16]. Finite element analyses of the DCB direct Mode I fracture tests in which sophisticated constitutive models for fiber reinforced polymer composites are employed have also been performed [17, 18, 19, 20]. The DCB direct Mode I fracture tests were also applied to engineering materials other than fiber reinforced polymer composites such as wood [21] and bovine bone tissue [22], as well as debonding of adhesively bonded joints that produced a significant literature (see e.g. [23]).

In all the aforementioned studies, the DCB loading configuration has been the separation of the cantilever beams at the free ends to produce Mode I fracture directly, similar to those of the standards ASTM D5528-13 [24], ISO 15024 [25] and JIS K7086 [26]. On the other hand, the conventional DCB loading configuration would result in two fundamental problems in the case of concrete: (1) Distributed cracking along the cantilever arms that dissipate

3

spurious energy becomes inevitable due to bending moment and shear, (2) the shear stresses acting in the fracture process zone cause the crack to curve instead of propagating in a straight line resulting in mixed mode fracture instead of Mode I fracture.

Thus, as the principal objective of this study size effect tests and fracturing analyses of DCB specimens made of plain normal and high strength concretes loaded to produce Mode I fracture *indirectly* are presented. In these tests, DCB specimens are supported eccentrically at the cantilever ends and loaded in compression resulting in bending moments in the DCB cantilever beam-columns as well as compressive stresses parallel to the initial notch. Moreover, the lack of shear in the cantilever arms allow the crack to grow in a straight line. In the light of the aforementioned studies on the fracture mechanics of the orthotropic polymer composite DCBs, larger bending stiffness for the cantilever columns are employed in order to obtain a straight crack path during the crack propagation in the concrete indirect tension DCB specimens [18].

In contrast to complex testing techniques in which crack mouth opening displacement (CMOD) or at least load point displacement (work of fracture method) is controlled for the purposes of the determination of material fracturing properties, the size effect method of fracture testing requires only the peak loads if the material strength is determined independently of the size effect tests and therefore there is no need for measuring CMODs or load point displacements. Further simplification of the testing procedure is made

possible by choosing a compression setup instead of a tension setup, even when Mode I fracture properties are pursued. Furthermore, the size effect curve yields information on the brittleness of the specimens but the work of fracture method does not. In the case of concretes, the size effect method was applied successfully to the failure of concrete structures failing in tension, in diagonal shear, in torsion [27, 28], in pull-out of reinforcing bars [29], in bond splice [30], in compression [31, 32, 33, 34], in bending [35, 36, 37] as well as by Arcan tests [38].

However, in the case of normal strength concretes, the specimen size range that can be successfully cast and tested in the laboratory is too small. Thus, as the secondary objective of this study, the errors in the predictions of size effect fracture parameters are investigated by introducing peak loads obtained by the finite element analyses with the Model M7 of *virtual* specimens in the size effect analyses. To this end, for each test series, one virtual specimen twice as large as the largest tested one (for which actual laboratory testing would be prohibitive) and one virtual specimen half the size of the smallest tested one have been analyzed by the model M7 to determine their peak loads. It is shown that these peak loads provide valuable data points that improve vastly the accuracy of the size effect curve in predicting the Type II size effect fracturing parameters. The existence of complex states of stress at the crack front in the indirect tension DCB specimen because of strain-softening resulting from distributed cracking, localization of cracking into a larger fracture zone prior to failure, and bridging stresses at the fracture front require

5

a sophisticated model for the analysis of the failure of indirect tension DCB specimens made of concrete [39]. The model M7 is one of the few models which satisfy these requirements. The so called "computational continuum models" (like the model M7, as opposed to "computational discrete models") must have an additional parameter considered to be a material property to control the localization of the strains, called the characteristic length or localization limiter. Both types of material models were shown to agree well with the size effect formulas fitted to the peak loads of geometrically similar specimens of a sufficiently broad size range [40, 41, 42, 43] obtained from size effect tests such as 3 point bending and uniaxial tension.

2. Size Effect Test Specimens and Experiments

Three series of normal and high strength concrete specimens were produced. Specimen thicknesses of $b = 30$, 40 and 50mm were chosen for series A, B and C respectively. All series have three different size of specimen and three specimens were cast for each size. Each series contained nine specimens; since all three series were produced using normal and high strength concrete, in total 54 specimens were cast. The initial letters of labels of specimens P and HS correspond to plain and high strength DCBs, and the letters A, B and C that follow P or HS correspond to each of the 3 series, and the numbers 1-3, 4-6, 7-9 correspond to three specimens that were tested in each series. For geometrical similarity, specimen dimensions were chosen so as to have a geometrical scaling of 1:2:4. The specimen geometries and dimensions

6

are shown in Fig.1.

The concrete mix proportions water:cement:sand:gravel were 0.55:1:2:2 by weight for the normal strength concrete and water : cement : sand : gravel : superplasticizer : silica fume were 0.35:1:2:2:0.015:0.11 by weight for the high strength concrete. Portland cement (KPC32.5, according to Turkish standard TS EN197-1), similar to ASTM Type I, and Kızılırmak river aggregate from the county of Kırıkkale were used. The maximum aggregate size was $d_a = 10$mm, the maximum sand size was 5mm for all the DCBs. All of the specimens were tested at the age of 90 days. The average 90-day compressive strengths together with their respective coefficients of variation are presented in Table 1. All of the specimens in all sizes for any given type of concrete were cast from the same batch of concrete. The DCBs were cast in forms made of plywood with a smooth hard varnish-painted surface. The DCB notches were obtained by introducing plastic plates at the notch locations while casting. The ratio of notch length to specimen height was chosen as $a/d = 0.6$. The forms were stripped after one day, and the specimens were cured for 28 days in water. Additionally, for each series a standard compression test specimen was cast from the same batch and cured for 28 days in water. At the end of the curing period, the specimens were kept at a temperature of 20°C and a relative humidity of 50% until the time of test.

The specimens were tested in a material testing machine with a stiffness constant of 560kN/mm in the Structure Laboratory of the Department of Civil Engineering at Gazi University, Ankara, Turkey. The stroke rate was

determined so as to achieve the maximum load for each specimen within about 3 min. The load measurements were taken from a load cell with 225kN capacity automatically using the closed loop testing system. Two horizontal displacements at the cantilever ends (LVDT1 and LVDT2) and one axial displacement (LVDT3) were measured by LVDT gauges. The maximum registered values from LVDT1 and LVDT2 were approximately 30mm for the largest specimen, 15mm for medium size specimen and 7.5mm for the smallest size specimen. Experimental setup is depicted in Fig. 2a.

The cantilever ends were loaded using steel plates which had a width of 20% of the cantilever width. The dimensions of the top support were twice that of the cantilever end supports. The same apparatus was used for all tests. The failure loads recorded in these tests for each specimen are shown in Table 2.

To determine the tensile strength of concrete, a series of uniaxial compression tests on standard cylindrical specimens are performed. Once the compressive strength is determined, the splitting tensile strength can be empirically determined using the formulae provided in various standards. In this study, the splitting tensile strengths f_{ct} for the two types of concretes are estimated empirically using both the ACI formula given by

$$f_{ct} = 0.56\sqrt{f_c'} \tag{1}$$

in which both strengths are expressed in MPa as well as the CEB-FIB formula

given by

$$f_{ct} = 0.3(f'_c)^{0.66} \tag{2}$$

in which again both strengths are expressed in MPa. The direct tension tensile strength f'_t is estimated as the 80% of these splitting tensile strengths [44, 45, 46] as shown in Table 1. The difference in predictions from these two formulas are less than 7%. Thus, in this study for the normal strength and high strength concretes the direct tension tensile strengths are estimated as $f'_t = 2.40$MPa and $f'_t = 3.20$MPa respectively.

3. A Brief Description of The Model M7

The Microplane Model M7 is the latest model among a series of models called the "microplane models" for predicting the multiaxial inelastic behavior of plain concrete developed in collaboration with Z. P. Bažant at Northwestern University. Developing a multiaxial constitutive model for concrete (and in general, for a class of materials called "geomaterials") is a formidable task because unlike common ductile metals, concrete in general has a very complex mechanical response that changes character as a function of the current and the past states of stress. As a result, unlike ductile metals, a simple uniaxial test is not sufficient to fully describe the mechanical behavior of concrete. In compression, the confining pressure plays a major role in the mechanical response of concrete [47, 43]. Thus, triaxial hydrostatic compression tests are necessary to describe the pressure sensitivity of the response. The unloading and reloading behaviors of concrete in cyclic compression,

cyclic tension and cyclic hydrostatic compression are also wildly different [47, 43]. As a result, cyclic compression and cyclic tension tests as well as cyclic hydrostatic compression tests are also needed. Thus, for a complete characterization of the mechanical behavior of concrete, at least tests of (1) uniaxial compression, (2) uniaxial tension, (3) uniaxial cyclic compression (4) uniaxial cyclic tension (5) hydrostatic compression (6) hydrostatic cyclic compression (7) triaxial compression at various confining pressures and (8) triaxial cyclic compression at these confining pressures are needed [48, 42].

The Model M7 has been shown to successfully predict a total 25 distinct data sets obtained at a wide range of load paths including the aforementioned tests and some unconventional nonproportional load paths with a vertex at the yield surface [42, 43]. The performance of the model in many different finite element analyses of concrete specimens tested under various load paths have also been excellent [43].

The Model M7 consists of constitutive laws are prescribed on various planes in material mesostructure called the "microplane" that relate stress and strain vectors on these planes. The integration of stress vectors expressed as functions of strain vectors acting on these planes yields the macroscopic stress tensor. To this end, the so-called "kinematic constraint" in which the strain tensor is projected onto microplanes of different orientations given by the unit normal vector $\vec{n}$ must be employed:

$$\epsilon_N = \epsilon_{ij} n_i n_j = \epsilon_{ij} N_{ij} \tag{3}$$

where repeated indices mean summation and the indices range from 1 to 3. An alternative approach would be the so-called "static constraint" in which instead of the strain tensor, the stress tensor is projected onto microplanes but this approach would be suitable for plastic behavior of ductile metals because it would not permit the modeling of the post peak strain softening behavior of quasibrittle materials like concrete. To model the shear behavior of concrete, a local coordinate system is defined on the microplanes given by the orthonormal vectors $\vec{n}, \vec{l}$ and $\vec{m}$ in which the normal stress and strain are referred to the vector $\vec{n}$ and shear strains and stresses are referred to the vectors $\vec{l}$ and $\vec{m}$. The projected shear strains then are given by

$$
\begin{aligned}
\epsilon_L &= \epsilon_{ij}\frac{1}{2}\left(n_i l_j + l_i n_j\right) = \epsilon_{ij}L_{ij} \\
\epsilon_M &= \epsilon_{ij}\frac{1}{2}\left(n_i m_j + m_i n_j\right) = \epsilon_{ij}M_{ij}
\end{aligned} \tag{4}
$$

Given the projected strains on a microplane as defined by Eqs.3 and 4, the corresponding normal and shear stresses can be evaluated using the prescribed microplane constitutive laws generically given by

$$
\begin{aligned}
\sigma_N &= \mathcal{F}_N\left(\epsilon_N, \sigma_V\right) \text{ for } \sigma_N^e > 0 \\
\sigma_V^- &= \mathcal{F}_V\left(\epsilon_V, \epsilon_I, \epsilon_{III}\right) \\
\sigma_D^- &= \mathcal{F}_D\left(\epsilon_D, \epsilon_V\right) \\
\sigma_N &= \sigma_V^- + \sigma_D^- \text{ for } \sigma_N^e < 0 \\
\tau_L &= \mathcal{F}_\tau\left(\sigma_N\right)\cos(\alpha)
\end{aligned} \tag{5}
$$

11

$$\tau_M = \mathcal{F}_\tau(\sigma_N)\sin(\alpha)$$

in which the functions $\mathcal{F}_N$, $\mathcal{F}_V$, $\mathcal{F}_D$ and $\mathcal{F}_\tau$ denote the microplane normal, volumetric, deviatoric and shear constitutive laws respectively; σ_N^e is the elastic microplane normal stress, ϵ_V is the volumetric strain, σ_V is the volumetric stress, ϵ_I is the maximum principal strain and ϵ_{III} is the minimum principal strain (for details see [42]). In Eqs.5 the arguments to the microplane constitutive functions turn out to be not only the corresponding microplane strains, but also other microplane stress variables [42], discovered through extensive data fitting involving numerous data sets on different concretes. This means a deviation from pure kinematic constraint towards static constraint, but this may be justified by the fact that the quasibrittle materials transition from brittle to ductile behavior as the confining pressure increases and thus at any given confining pressure the material behavior must be conforming partly to the kinematic constraint and partly to the static constraint. The microplane shear law is effectively a yield surface which helps simulate the plastic behavior of concrete under triaxial compression. To calculate the macroscopic stress tensor without introducing any spurious anisotropy, the microplane normal and shear stresses given in Eqs.5 are integrated over the surface of a unit hemisphere using the principle of virtual work:

$$\sigma_{ij} = \frac{3}{2\pi} \int_S \left(\sigma_N N_{ij} + \tau_L L_{ij} + \tau_M M_{ij} \right) \mathrm{d}S \tag{6}$$

12

The integral in Eq.6 is evaluated numerically using the Gaussian quadrature for best efficiency and accuracy. Although as low as 21 points can be used to get an approximately isotropic response, in the post peak region of the stress-strain response the error in isotropy may become too large [48]. Thus, a 37 point Gaussian quadrature is employed in the calculations, which allows the complete stress-strain response to be approximately isotropic [42].

Most of the foregoing equations are common to the Model M7 and its many predecessors (models called M1 [49] through M6f [50]). However, the Model M7 outperforms its predecessors by (1) predicting correctly the tensile and compressive behavior of concrete under loading and unloading cycles *in addition to* predicting correctly other concrete multiaxial behavior, (2) predicting correctly the lateral contraction in uniaxial tension. None of its predecessors could predict correctly either such cyclic behavior of concrete or the lateral contraction under tension with the exception of the early predecessors (e.g. the Model M1 [49]) which, on the other hand, could *not at all* predict correctly multiaxial compressive behavior of concrete.

To accomplish the correct predictions of concrete behavior under such load cycles as well as the correct prediction of lateral contraction under uniaxial tension, the Model M7 uses the so-called volumetric-deviatoric split in microplane normal stress and strain in the inelastic range of response in compression as shown in Eqs.5 but the normal stress and strain without split in both elastic and inelastic ranges of tensile response. Moreover, the model M7 features about the same number of fixed and free parameters as

13

its more recent predecessors (e.g. the Model M4 [48, 47]). Clearly, among the microplane models with a sound, noncontroversial theoretical basis ever published, the Model M7 is arguably the best microplane model for concrete. However, the versatility in data fitting provided by prescribing the constitutive law at microplane level make a direct relation between the size effect fracturing parameters and the parameters of the Model M7 impossible.

4. Size Effect Fracture Analyses and Results

The calibration of the Model M7 is of profound importance to be able to accurately predict the size effect fracture parameters B, d_0, c_f and G_f of both the normal strength and the high strength concretes employed in the tests using the size effect analyses. To this end, the elastic moduli for the normal and high strength concretes were prescribed as $E = 27109$MPa and $E = 33711$MPa and the Model M7 was calibrated by varying the free parameters k_1 and k_3 to match the compressive strength obtained by the uniaxial compression test for the concrete from each series. Thus, the optimum values of these parameters turn out to be $k_1 = 75 \cdot 10^{-6}$ and $k_3 = 33.0$ for the normal strength concrete and $k_1 = 75 \cdot 10^{-6}$ and $k_3 = 53.0$ for the high strength concrete. In Fig.3, the effect of a varying k_1 on the tensile response of the Model M7 is shown. The curve in the middle corresponds to the calibrated $k_1 = 75 \cdot 10^{-6}$ value. The upper curve corresponds to $k_1 = 112.5 \cdot 10^{-6}$ which is 50% higher than the calibrated value. The lower curve is for $k_1 = 37.5 \cdot 10^{-6}$ which is 50% of the calibrated k_1. Clearly by varying the free parameter k_1,

14

the response is scaled radially and as a result, the response curve has the same relative proportions. Thus, calibration of the Model M7 independently of the failure loads of the geometrically similar specimens by varying only the free parameters of the model allows the equivalent cohesive curve to be uniquely defined [51].

The Type II size effect analysis begins with using the failure loads P_u given in Table 2 to calculate the nominal strengths as $\sigma_{Nu} = P_u/bd$ where b is the width (out of plane dimension) of the specimen and d is the height of the specimen as shown in Fig.2b for 2D geometric similarity. For small enough size DCB specimens, the nominal strength is expected to approach a horizontal asymptote (or constant strength) and for large enough size DCB specimens, it should approach the LEFM asymptote with a $-1/2$ slope in the log-log scale. The simplest formula that satisfies both conditions may be written as [40]:

$$\sigma_{Nu} = \frac{Bf'_t}{\sqrt{(1 + d/d_0)}} = \frac{\sqrt{E'G_f/g'_0 c_f}}{\sqrt{1 + g_0 d/g'_0 c_f}} \qquad (7)$$

where Bf'_t is the value of the horizontal asymptote in the small size limit, f'_t is the tensile strength of concrete, G_f is the fracture energy of concrete, $a_{eff} = a_0 + c_f$ is the effective crack length at failure in which a_0 is the notch length and c_f is the half of the size of the fracture process zone, $g_0 = g(a_0/d)$ is the energy release rate function, $g'_0 = g'(a_0/d)$, $E' = E =$ the elastic modulus for plane stress and d_0 is the transitional size between the brittle

15

and non brittle behavior for the concrete under consideration.

Optimal fitting of Eq.7 to the test data shown in Table 2 reveals the size effect fracture parameters as shown in Table 3 for all test series. The test data and their optimal size effect curves are plotted in Fig.4. To obtain the fracture parameters c_f and G_f, using Eq.7 one can derive Eqs. 8 and 9 [40] given by

$$\frac{1}{d_0} = \frac{g_0}{g'_0 c_f} \tag{8}$$

$$Bf'_t = \sqrt{\frac{E'G_f}{g'_0 c_f}} \tag{9}$$

and substituting $c_f = g_0 d_0 / g'_0$ from Eq.8 in Eq.9 one obtains

$$G_f = (Bf'_t)^2 \frac{g_0 d_0}{E'} \tag{10}$$

As shown in Fig.2b, the nondimensional notch length is given as $\bar{a}_0 = a_0/d = 0.6$, the nondimensional half size of the fracture process zone to be determined from size effect analysis as $\Delta\bar{a} = \Delta a/d$, the nondimensional width of the specimen as $2\bar{c} = 2c/d \approx 0.85$, the nondimensional eccentricity as $\bar{e} = e/d = \bar{c}/5 \approx 0.085$, the nondimensional notch width as $\bar{\lambda} = \lambda/d$ which varied between 0.0167 and 0.0667 because of a constant 5mm notch width employed in all specimens. The nondimensional load is defined as $\bar{P} = P/Ed^2$. In the foregoing equations, E is the Young's modulus and d is the depth of the geometrically similar DCB specimens tested. The nondimensional

16

thicknesses of the specimens $\bar{b} = b/d$ also varied between 0.1 and 0.4. It is assumed that both the nondimensional notch width and the nondimensional thickness not being constants has negligible effect on the results. The energy release rate function $g_0 = g(0.6)$ and its derivative $g'_0 = g'(0.6)$ in the foregoing equations are to be determined for the loading configuration, shape and geometry of the specimen as given above. To this end, the energy release rate determined from the complementary strain energy $U^* = P^2 C(a)/2$ at constant load is employed:

$$\mathcal{G} = \frac{1}{b}\frac{\mathrm{d}}{\mathrm{d}a}\left[\frac{1}{2}P^2 C(a)\right] \tag{11}$$

$$\Rightarrow \mathcal{G} = \frac{1}{2b}\frac{P^2}{d}C'(\bar{a}) \tag{12}$$

where $C(a)$ is the compliance of the structure, i.e. $u = C(a)P$ in which u is the load point displacement and P is the load. The stress intensity factor K_I may be expressed as

$$K_I = \sigma_N\sqrt{d}\sqrt{g(\bar{a})} = \sqrt{E'\mathcal{G}} \tag{13}$$

where $\sigma_N = P/bd$ is the nominal stress. Substituting $\mathcal{G}$ from Eq.12 into Eq.13 and solving for $g(\bar{a})$ one may obtain

$$g(\bar{a}) = \frac{1}{2}E'bC'(\bar{a}) \tag{14}$$

$$\Rightarrow g'(\bar{a}) = \frac{1}{2}E'bC''(\bar{a}) \tag{15}$$

17

Thus, to determine $g_0 = g(\bar{a}_0) = g(0.6)$ one must determine $C'(0.6)$ and substitute this value in Eq.14. Similarly, to determine $g_0' = g'(\bar{a}_0) = g'(0.6)$ one must determine $C''(0.6)$ and substitute it in Eq.15. In this study the first and second derivatives of the compliance function are determined through the finite difference method, which produces highly accurate results [40]:

$$C'(\bar{a}_0) \approx \frac{C\left(\bar{a}_0 + \Delta\bar{a}_0\right) - C\left(\bar{a}_0 - \Delta\bar{a}_0\right)}{2\Delta\bar{a}_0} \tag{16}$$

$$C''(\bar{a}_0) \approx \frac{C\left(\bar{a}_0 + \Delta\bar{a}_0\right) - 2C\left(\bar{a}_0\right) + C\left(\bar{a}_0 - \Delta\bar{a}_0\right)}{\left(\Delta\bar{a}_0\right)^2} \tag{17}$$

where $\bar{a}_0 = 0.6$ and $\Delta\bar{a}_0$ is suitably chosen to be 0.01. The compliances appearing in Eqs.16 and 17 are then determined through linear elastic finite element analyses employing 278400, 272000 and 268800 hexahedral elements of type C3D8R of ABAQUS [52] for series A, B and C of the DCB specimens respectively. The nondimensional compliance values obtained in these analyses for series A specimens are $C(0.59) = 51.559$, $C(0.60) = 52.140$ and $C(0.61) = 52.772$ which yield $C'(0.6) = 60.610$ and $C''(0.6) = 506.00$. Thus, $g_0(0.6)$ and $g_0'(0.6)$ turn out to be 3.031 and 25.300 respectively for this series of DCB specimens.

In Fig.4(a) through (c) the size effect fits for each one of the series PA, PB and PC DCB specimens are shown. Similarly, in Figs.4(e) through (g) the size effect fits for each one of the series HSA, HSB and HSC DCB specimens are given. In Fig.4(d) and Fig.4(h) the size effect fits for all nominal strength data obtained by testing respectively normal strength and high strength DCB

18

specimens are shown. These size effect analyses of the peak loads yield the size effect fracture parameter values as given in Table 3 for all test series.

The proposed experimental method would be incomplete unless the errors in the size effect fracture parameters are estimated by carrying out a comparison of the results, namely Bf_t', d_0, c_f and G_f, obtained from Type II size effect analyses of the peak loads from the tested specimens only with those obtained from the same analyses applied to the predicted peak loads from the virtual specimens. To this end, a virtual DCB specimen half the size of the smallest tested DCB specimen and a twice as large as the largest tested one are proposed for each test series. The sizes of these virtual specimens are determined based on not only the computational feasibility of the finite element analyses of the large size virtual specimens but also on the previous data fitting experience with the Model M7 and the minimum permissible element density in the small size virtual specimens. After calibrating the Model M7 for the two types of concretes employed in the tests, the peak loads of all virtual DCB specimens from all series are determined using finite element analyses in which the Model M7 is used as the constitutive law. As the finite element driver, the commercial finite element analysis package ABAQUS version 2016 is employed [52]. The analyses are performed in the sense of crack band model in which the element width is chosen as 2.5mm for the both normal and high strength concretes.

The predicted peak loads for these virtual DCB specimens and their optimally fitting size effect curves are shown in Fig.5. For comparison, the

experimental peak loads are also shown in the same figure. The optimum values of the size effect fracturing parameters Bf_t', d_0, c_f, G_f and B obtained by these optimal fits are given in Table 4 for each test series as well as for all normal strength and for all high strength series.

Comparing Tables 3 and 4 it may be inferred that the experimental data alone give rise to a large scatter in the size effect fracture parameters, which may be due to inherent statistical scatter in concrete. The size effect analysis of the predicted peak loads by the Model M7 allows the errors in the fracture size effect parameters obtained using the experiments to be determined. The errors in the fracture parameters Bf_t', d_0, c_f, G_f and B obtained using the peak loads from the tests only relative to those obtained using the predicted peak loads from the virtual experiments turn out to be 18.207%, 48.150%, 48.150%, 27.550% and 18.207% for all P-series and 1.664%, 0.344%, 0.344%, 3.000% and 1.664% for all HS-series respectively. Thus, it may be concluded that when the material microstructure is large, the size range that can possibly be tested in the laboratory is likely to be too small compared to the material microstructure size and the guidance of a well established material model is needed to obtain reasonable estimates of fracture parameters using the size effect analysis.

In Figs. 6a-e and 7a-e the cracking patterns of the normal strength and high strength series C DCB specimens are shown respectively. The crack propagation is illustrated as the maximum principal logarithmic strain immediately before and immediately after the peak load for each specimen. The

20

smallest virtual specimens have the sizes 37.5mm, 50mm and 62.5mm for series A, B and C respectively. The largest virtual specimens have the sizes 600mm, 800mm, 1000mm for series A, B and C respectively. Keeping the element size constant in the sense of crack band model, the normal strength and high strength series C DCB specimens shown in Figs. 6a-e and 7a-e are meshed using 1430, 5500, 21000, 84000, and 336000 8-node brick elements of type C3D8R. On the right column in the Figs.6 and 7 the half of the size of the fracture process zone c_f is also drawn scaled relative to the size of each DCB specimen. Clearly for the largest virtual DCB specimens, c_f becomes negligibly small.

5. Conclusions

Test results from a novel DCB indirect Mode I test in which geometrically similar specimens are supported at the cantilever beam-column free ends eccentrically and loaded in compression in the direction of their notches are reported. Using a sophisticated multiaxial constitutive model for concrete, called the Microplane Model M7 calibrated independently of size effect test data for the normal and high strength concretes employed in the experiments, the experimentally obtained peak loads are predicted. Furthermore, the peak loads of geometrically similar one virtual DCB specimen twice as large as the largest tested DCB specimen and one virtual DCB specimen half the size of the smallest tested DCB specimens in each series are determined using the Model M7. The size effect fracture parameters, namely c_f, G_f, B and d_0 are

21

calculated applying the so-called Bažant's Type II Size Effect Law [41] to peak loads from experiments and to predicted peak loads from virtual tests. Consequently, the following conclusions may be drawn in this study:

1. The specimens tested have failed in Mode I. A relatively straight crack propagated from the notch tip toward the load point and broke the specimen into two pieces in all specimens.

2. A strong size effect is observed in the failure loads obtained from the tests and it follows the so called Type II size effect law.

3. The size effect fracture parameters obtained from the failure loads predicted by the Model M7 of geometrically similar virtual DCB specimens may be compared to those obtained from the peak loads from the experiments which allows the errors in these experimental results to be estimated.

4. Type II size effect analyses of the experimental failure loads alone yield a G_f for normal strength concrete about 29% higher than that for the high strength concrete. However, when the predicted failure loads from virtual DCB tests are employed, the Type II size effect analyses yield a G_f for high strength concrete higher than that for normal strength concrete but only by about 11%.

5. In the case of normal strength concrete, the DCB size range tested in the laboratory remained too small compared to the characteristic size of the material and this lead to errors in excess of 45% in the predicted c_f and over 25% in the predicted G_f and in the case of high strength

concrete, these errors respectively are over 0.34% and about 3%.

6. In contrast to the work of fracture method (in which the full load vs load point displacement diagram must be traced without any snap-back instabilities to yield the two fracture parameters), the proposed DCB indirect Mode I fracture testing method in which only the failure loads in compression of geometrically similar DCB specimens are determined to yield the fracture parameters is vastly simpler.

7. The Model M7 must be calibrated independently of the peak loads obtained in the size effect tests using only the free parameters of the model. The simplest calibration of the model may be to fit the compressive strength obtained by simple uniaxial compression tests.

6. Acknowledgements

7. Figures

Figure 1: The DCB specimens form the series A, B and C and their dimensions given in mm.

Figure 2: a) The schematic description of the test setup where dimensions of the support detail are given in mm, b) the dimensions and loading configuration of the indirect tension DCB specimen in nondimensional space.

Figure 3: Radial scaling of tensile response by varying the free parameter k_1 in (a) normal strength concrete, (b) high strength concrete. The dashed curves correspond to 50% higher and 50% lower values of k_1. The solid curves are for the calibrated value of $k_1 = 75 \cdot 10^{-6}$.

Figure 4: Type II size effect fits on the nominal strength of tested DCB specimens for both the normal strength (a-c) and the high strength concretes (e-g) for each of the series A, B and C as well as for all normal strength DCB specimens (d) and for all high strength DCB specimens (h).

Figure 5: Type II size effect fits on the nominal strength of the virtual specimens analyzed by the Model M7 for both the normal strength (a-c) and the high strength concretes (e-g) for each of the series A, B and C as well as for all normal strength DCB specimens (d) and for all high strength DCB specimens (h).

Figure 6: Fracture patterns of DCB specimens for the normal strength concrete specimen sizes of a) $d = 62.5$mm, b) $d = 125$mm, c) $d = 250$mm, d) $d = 500$mm, e) $d = 1000$mm obtained using the Microplane Model M7. On the right column c_f is drawn relative to the specimen size on each specimen.

Figure 7: Fracture patterns of DCB specimens for the high strength concrete specimen sizes of a) $d = 62.5$mm, b) $d = 125$mm, c) $d = 250$mm, d) $d = 500$mm, e) $d = 1000$mm obtained using the Microplane Model M7. On the right column c_f is drawn relative to the specimen size on each specimen.

8. Tables

DCB designation	Compressive strength (MPa)	Coefficient of variation on compressive strength	$f'_t = 0.8 f_{ct}$ from ACI formula (MPa)	$f'_t = 0.8 f_{ct}$ from CEB-FIB formula (MPa)
PA, PB, PC	32.78	5.9%	2.57	2.40
HSA, HSB, HSC	50.69	8.6%	3.19	3.20

Table 1: The compressive strengths obtained from uniaxial compression tests of standard cylinders and direct tension tensile strengths obtained as 80% of the splitting tensile strengths given by ACI and CEB-FIB formulas.

DCB specimen	Failure load in kN	DCB specimen	Failure load in kN
PA1	8.612	HSA1	9.091
PA2	8.708	HSA2	11.005
PA3	8.134	HSA3	13.493
PA4	4.211	HSA4	7.656
PA5	5.455	HSA5	7.273
PA6	5.933	HSA6	6.699
PA7	2.775	HSA7	5.550
PA8	3.445	HSA8	2.967
PA9	2.297	HSA9	4.211
PB1	18.373	HSB1	16.364
PB2	20.479	HSB2	14.928
PB3	10.048	HSB3	18.373
PB4	8.900	HSB4	8.612
PB5	6.124	HSB5	9.378
PB6	11.675	HSB6	12.919
PB7	4.019	HSB7	5.646
PB8	7.368	HSB8	5.933
PB9	3.732	HSB9	5.359
PC1	23.828	HSC1	22.871
PC2	18.852	HSC2	22.704
PC3	20.574	HSC3	23.349
PC4	11.483	HSC4	12.919
PC5	10.335	HSC5	13.493
PC6	8.900	HSC6	18.565
PC7	6.603	HSC7	7.847
PC8	6.794	HSC8	6.890
PC9	5.742	HSC9	5.646

Table 2: The failure loads of all DCB specimens tested in series A, B and C. The prefix "P" means normal strength concrete and "HS" means high strength concrete.

Test series		Bf'_t (MPa)	d_0 (mm)	c_f (mm)	G_f (N/mm)	B
PA		1.466	214.582	25.703	0.052	0.611
PB		1.399	451.081	53.934	0.094	0.583
PC		1.098	723.572	86.836	0.091	0.458
All series	P-	1.452	255.523	30.608	0.058	0.605
HSA		2.528	90.950	10.894	0.052	0.790
HSB		1.717	228.900	27.369	0.058	0.537
HSC		1.162	878.118	105.384	0.099	0.363
All series	HS-	2.144	114.064	13.663	0.045	0.670

Table 3: The results of fitting $\sigma_{Nu} = Bf'_t/\sqrt{1 + d/d_0}$ to the experimentally obtained nominal strength of DCB specimens from series A, B and C for normal and high strength concretes

Test series		Bf'_t (MPa)	d_0 (mm)	c_f (mm)	G_f (N/mm)	B
PA		1.807	114.074	13.664	0.042	0.753
PB		1.716	133.192	15.925	0.042	0.715
PC		1.703	127.516	15.303	0.038	0.709
All series	P-	1.717	132.490	15.870	0.042	0.715
HSA		2.175	119.681	14.336	0.051	0.680
HSB		2.128	120.847	14.449	0.047	0.665
HSC		2.172	103.336	12.401	0.041	0.679
All series	HS-	2.179	113.671	13.616	0.047	0.681

Table 4: The results of fitting $\sigma_{Nu} = Bf'_t/\sqrt{1 + d/d_0}$ to the nominal strength of the virtual DCB specimens predicted by the Model M7 of series A, B and C for normal and high strength concretes.

9. References

References

[1] R. Hoagland, "On the use of the double cantilever beam specimen for determining the plane strain fracture toughness of metals," *Journal of Basic Engineering*, vol. 89, no. 3, pp. 525–532, 1967.

[2] R. Heady, "Evaluation of sulfide corrosion cracking resistance in low alloy steels," *Corrosion*, vol. 33, no. 3, pp. 98–107, 1977.

[3] M. Kanninen, "An augmented double cantilever beam model for studying crack propagation and arrest," *International Journal of fracture*, vol. 9, no. 1, pp. 83–92, 1973.

[4] M. Kanninen, "A dynamic analysis of unstable crack propagation and arrest in the dcb test specimen," *International Journal of Fracture*, vol. 10, no. 3, pp. 415–430, 1974.

[5] J. Whitney, "Stress analysis of the double cantilever beam specimen," *Composites Science and Technology*, vol. 23, no. 3, pp. 201–219, 1985.

[6] L. Freund, "A simple model of the double cantilever beam crack propagation specimen," *Journal of the Mechanics and Physics of Solids*, vol. 25, no. 1, pp. 69–79, 1977.

[7] J. Williams, "End corrections for orthotropic dcb specimens," *Composites Science and Technology*, vol. 35, no. 4, pp. 367–376, 1989.

[8] S. Hashemi, A. Kinloch, and J. Williams, "Corrections needed in double-cantilever beam tests for assessing the interlaminar failure of fibre-composites," *Journal of Materials Science Letters*, vol. 8, no. 2, pp. 125–129, 1989.

[9] K. Kondo, "Analysis of double cantilever beam specimen," *Advanced Composite Materials*, vol. 4, no. 4, pp. 355–366, 1995.

[10] B. Blackman, H. Hadavinia, A. Kinloch, M. Paraschi, and J. Williams, "The calculation of adhesive fracture energies in Mode I: revisiting the tapered double cantilever beam (tdcb) test," *Engineering Fracture Mechanics*, vol. 70, no. 2, pp. 233–248, 2003.

[11] M. Shokrieh, M. Heidari-Rarani, and M. Ayatollahi, "Calculation of g_i for a multidirectional composite double cantilever beam on two-parametric elastic foundation," *Aerospace Science and Technology*, vol. 15, no. 7, pp. 534–543, 2011.

[12] M. Shokrieh and A. Zeinedini, "A novel method for calculation of strain energy release rate of asymmetric double cantilever laminated composite beams," *Applied Composite Materials*, vol. 21, no. 3, pp. 399–415, 2014.

[13] D. Nicholls and J. Gallagher, "Determination of g_{Ic} in angle ply composites using a cantilever beam test method," *Journal of Reinforced Plastics and Composites*, vol. 2, no. 1, pp. 2–17, 1983.

[14] B. Davidson, "An analytical investigation of delamination front curvature in double cantilever beam specimens," *Journal of Composite Materials*, vol. 24, no. 11, pp. 1124–1137, 1990.

[15] B. N. Rao and A. Acharya, "Evaluation of fracture energy g_{Ic} using a double cantilever beam fibre composite specimen," *Engineering Fracture Mechanics*, vol. 51, no. 2, pp. 317–322, 1995.

[16] A. B. de Morais, "Double cantilever beam testing of multidirectional laminates," *Composites Part A: Applied Science and Manufacturing*, vol. 34, no. 12, pp. 1135–1142, 2003.

[17] A. De Morais, M. De Moura, J. Gonçalves, and P. Camanho, "Analysis of crack propagation in double cantilever beam tests of multidirectional laminates," *Mechanics of Materials*, vol. 35, no. 7, pp. 641–652, 2003.

[18] T. Sebaey, N. Blanco, C. Lopes, and J. Costa, "Numerical investigation to prevent crack jumping in double cantilever beam tests of multidirectional composite laminates," *Composites Science and Technology*, vol. 71, no. 13, pp. 1587–1592, 2011.

[19] A. De Morais, "A new fibre bridging based analysis of the double cantilever beam (dcb) test," *Composites Part A: Applied Science and Manufacturing*, vol. 42, no. 10, pp. 1361–1368, 2011.

[20] B. Krull, J. Patrick, K. Hart, S. White, and N. Sottos, "Automatic opti-

cal crack tracking for double cantilever beam specimens," *Experimental Techniques*, vol. 40, no. 3, pp. 937–945, 2016.

[21] M. De Moura, J. Morais, and N. Dourado, "A new data reduction scheme for Mode I wood fracture characterization using the double cantilever beam test," *Engineering Fracture Mechanics*, vol. 75, no. 13, pp. 3852–3865, 2008.

[22] J. Morais, M. de Moura, F. Pereira, J. Xavier, D. N., and J. Dias, M.I.R.and Azevedo, "The double cantilever beam test applied to Mode I fracture characterization of cortical bone tissue," *Journal of the Mechanical Behavior of Biomedical Materials*, vol. 3, no. 6, pp. 446–453, 2010.

[23] R. Dimitri, P. Cornetti, V. Mantič, and L. de Lorenzis, "Mode I debonding of a double cantilever beam: A comparison between cohesive crack modeling and finite fracture mechanics," *Int. J. of Solids and Structures*, vol. 124, pp. 57–72, 2017.

[24] ASTM Standard D5528-13, "Standard test method for Mode I interlaminar fracture toughness of unidirectional fiber-reinforced polymer matrix composites," 2013.

[25] ISO 15024, "Fibre-reinforced plastic composites - determination of Mode I interlaminar fracture toughness, g_{Ic}, for unidirectionally reinforced materials," 2001.

[26] JIS K 7086, "Testing methods for interlaminar fracture toughness of carbon fibre reinforced plastics," 1993.

[27] Z. P. Bažant and S. Şener, "Size effect in torsional failure of concrete beams," *Journal of Structural Engineering*, vol. 113, no. 10, pp. 2125–2136, 1987.

[28] Z. P. Bažant, S. Şener, and P. C. Prat, "Size effect tests of torsional failure of plain and reinforced concrete beams," *Materials and Structures*, vol. 21, no. 6, p. 425, 1988.

[29] Z. P. Bažant and S. Şener, "Size effect in pullout tests," *ACI Materials Journal*, vol. 85, no. 5, pp. 347–351, 1988.

[30] S. Şener, Z. P. Bažant, and E. Becq-Giraudon, "Size effect on failure of bond splices of steel bars in concrete beams," *Journal of Structural Engineering*, vol. 125, no. 6, pp. 653–660, 1999.

[31] B. I. Barr, H. F. Abusiaf, and S. Sener, "Size effect and fracture energy studies using compact compression specimens," *Materials and Structures*, vol. 31, no. 1, p. 36, 1998.

[32] S. Sener, B. Barr, and H. Abusiaf, "Size-effect tests in unreinforced concrete," *Magazine of Concrete Research*, vol. 51, no. 1, pp. 3–11, 1999.

[33] S. Şener, B. I. Barr, and H. F. Abusiaf, "Size effect in axially loaded reinforced concrete columns," *Journal of Structural Engineering*, vol. 130, no. 4, pp. 662–670, 2004.

[34] V. Koç and S. Şener, "Size effect in normal-and high-strength concrete with different notches under the axial load," *Journal of Materials in Civil Engineering*, vol. 21, no. 9, pp. 433–445, 2009.

[35] Ç. Belgin and S. Şener, "Size effect on failure of overreinforced concrete beams," *Engineering Fracture Mechanics*, vol. 75, pp. 2308–2319, 2008.

[36] Y. Çağlar and S. Şener, "Size effect tests of different notch depth specimens with support rotation measurements," *Engineering Fracture Mechanics*, vol. 157, pp. 43–55, 2016.

[37] S. Şener and K. C. Şener, "Universal size effect of concrete specimens and effect of notch depth," *Challenge Journal of Structural Mechanics*, vol. 3, no. 1, pp. 47–51, 2017.

[38] S. Şener, Y. Çağlar, Ç. M. Belgin, and K. C. Şener, "Modified Arcan tests for concrete with multiwalled carbon nanotubes," *Advanced Materials Letter*, vol. 5, no. 8, pp. 429–434, 2014.

[39] Z. P. Bažant and Y. Xi, "Statistical size effect in quasi-brittle structures: Ii. nonlocal theory," *Journal of Engineering Mechanics*, vol. 117, no. 11, pp. 2623–2640, 1991.

[40] Z. Bažant and J. Planas, *Fracture and size effect in concrete and other quasibrittle materials*. CRC Press, London, 1997.

[41] Z. P. Bažant, *Scaling of structural strength*. Hermes- Penton Science Ltd., London, 2005.

[42] F. C. Caner and Z. P. Bažant, "Microplane model M7 for plain concrete. I: Formulation," *Journal of Engineering Mechanics*, vol. 139, no. 12, pp. 1714–1723, 2012.

[43] F. C. Caner and Z. P. Bažant, "Microplane model M7 for plain concrete. II: Calibration and verification," *Journal of Engineering Mechanics*, vol. 139, no. 12, pp. 1724–1735, 2013.

[44] T. Aly and J. G. Sanjayan, "Factors contributing to early age shrinkage cracking of slag concretes subjected to 7-days moist curing," *Materials and Structures*, vol. 41, no. 4, pp. 633–642, 2008.

[45] S. A. Altoubat and D. A. Lange, "Tensile basic creep: measurements and behavior at early age," *Urbana*, vol. 51, p. 61801, 2001.

[46] Y. Wei and W. Hansen, "Tensile creep behavior of concrete subject to constant restraint at very early ages," *Journal of Materials in Civil Engineering*, vol. 25, no. 9, pp. 1277–1284, 2012.

[47] F. C. Caner and Z. P. Bažant, "Microplane model M4 for concrete. II: Algorithm and calibration," *Journal of Engineering Mechanics*, vol. 126, no. 9, pp. 954–961, 2000.

[48] Z. P. Bažant, F. C. Caner, I. Carol, M. D. Adley, and S. A. Akers, "Microplane model M4 for concrete. I: Formulation with work-conjugate deviatoric stress," *Journal of Engineering Mechanics*, vol. 126, no. 9, pp. 944–953, 2000.

34

[49] Z. P. Bažant and B.-Y. Oh, "Microplane model for progressive fracture of concrete and rock," *J. of Engineering Mechanics*, vol. 111, pp. 559–582, 1985.

[50] F. Caner and Z. P. Bažant, "Microplane model M6f for fiber reinforced concrete," *Proceedings of the 11th Int. Conf. on Computational Plasticity. Fundamentals and Applications (Complas 11)*, 2012.

[51] Z. P. Bažant and Q. Yu, "Size-effect testing of cohesive fracture parameters and nonuniqueness of work-of-fracture method," *Journal of Engineering Mechanics*, vol. 137, no. 8, pp. 580–588, 2011.

[52] Simulia, "Abaqus/Explicit version 2016," *Dassault Systèmes*, 2016.
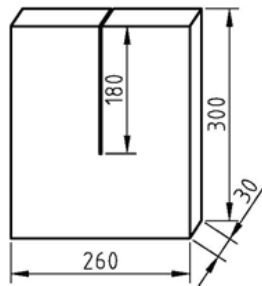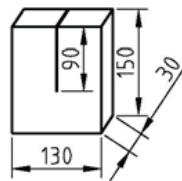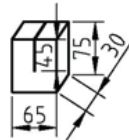
Figure(s)

A1 - A3   A4 - A6   A7 - A9
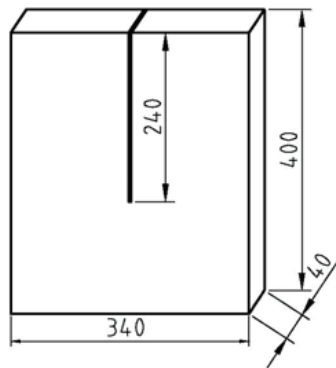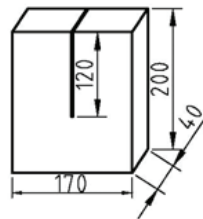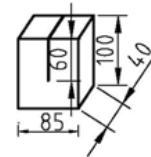
B1 - B3   B4 - B6   B7 - B9

C1 - C3   C4 - C6   C7 - C9

Figure(s)

a)

wire

D=18

LVDT1

LVDT2

LVDT3

1 2
4

b)

$\bar{P}$

$\bar{c}$

$\bar{c}$

$\bar{d}=1$

$\Delta\bar{a}$

$\bar{\lambda}$

$\bar{a}_0$

$\bar{e}$

$\bar{c}/2$

$\bar{c}/2$

$\bar{e}$

$\bar{P}/2$

$\bar{P}/2$

a) Normal Strength Series

b) High Strength Series

a)

b)

c)

d)

e)

Figure(s)

a)
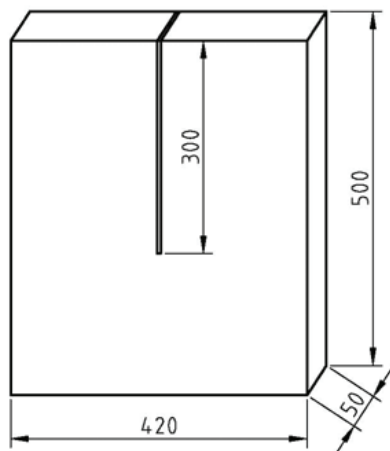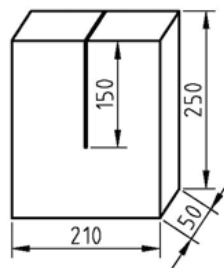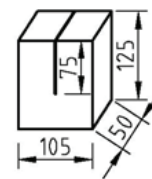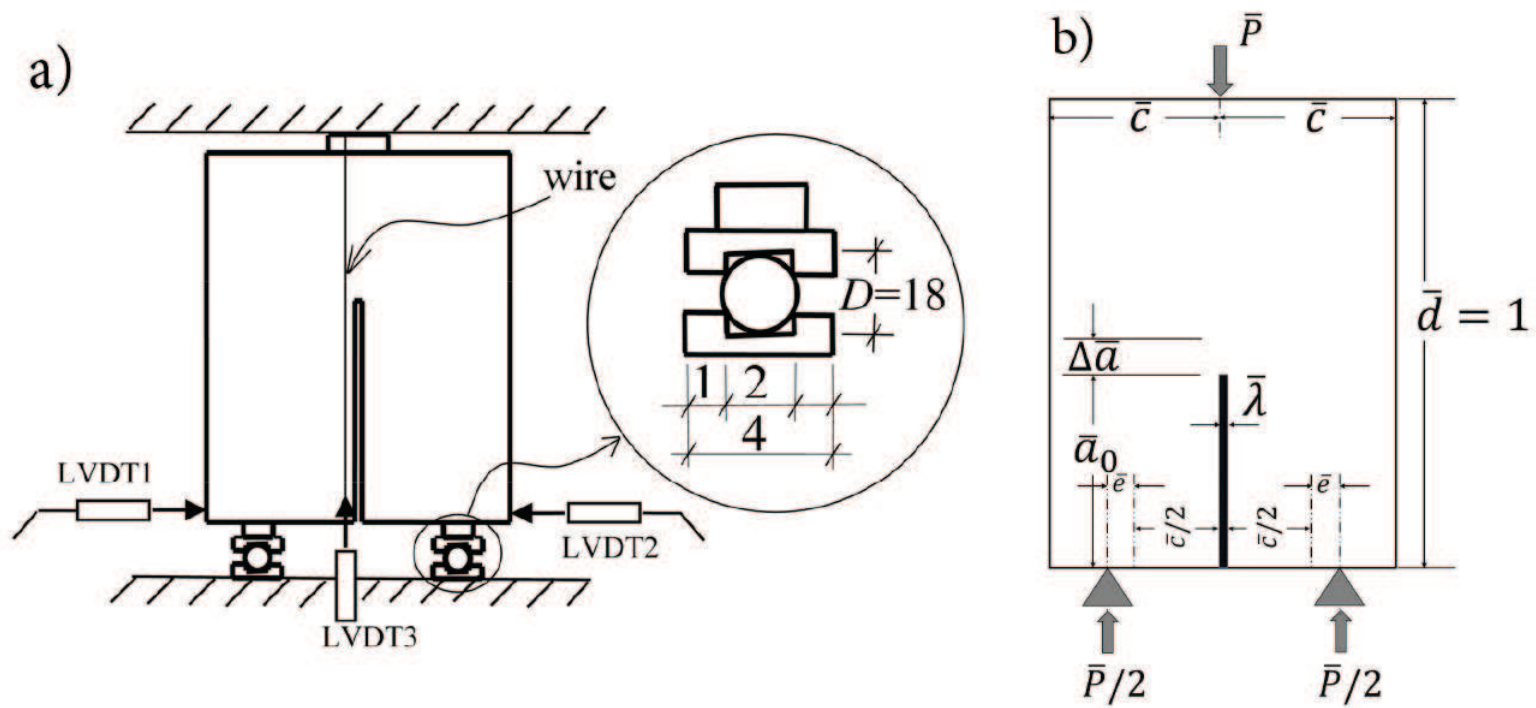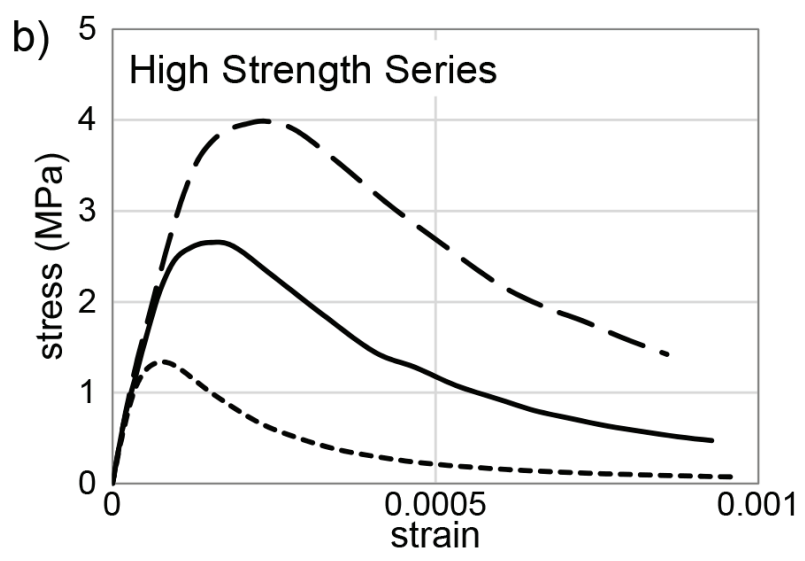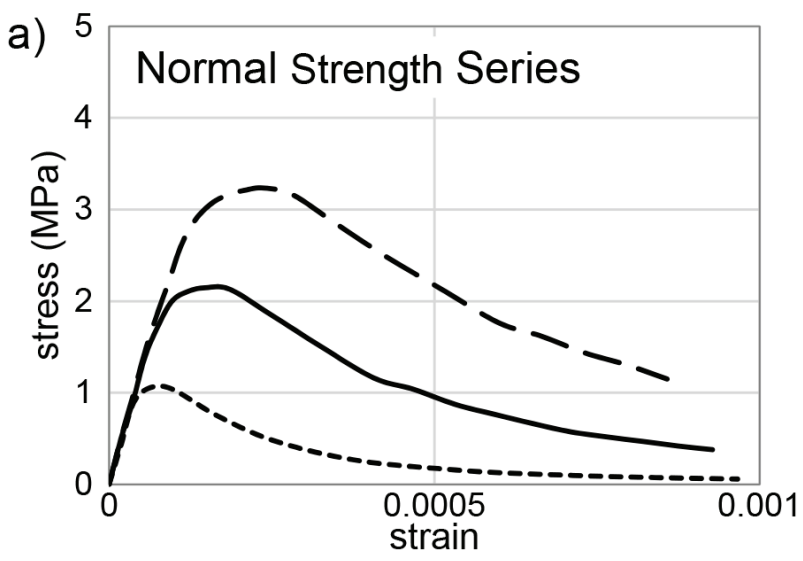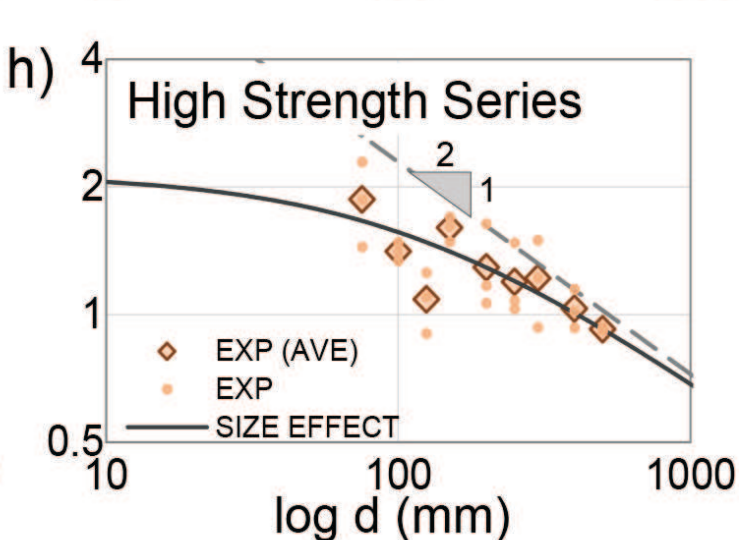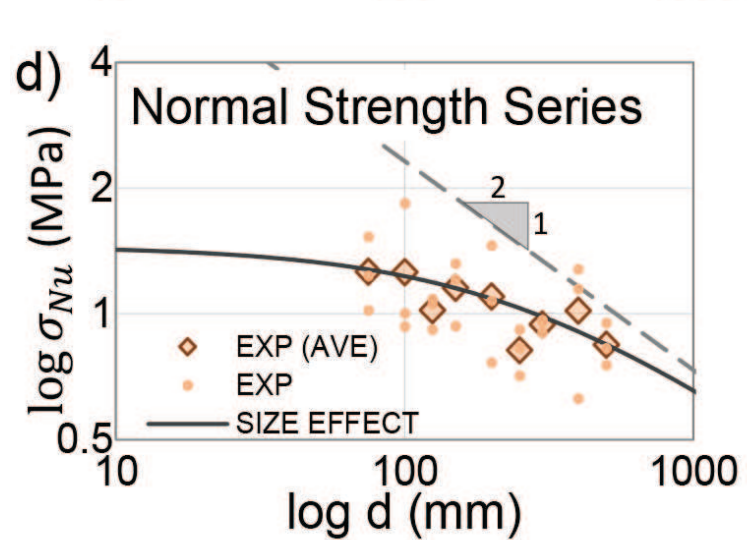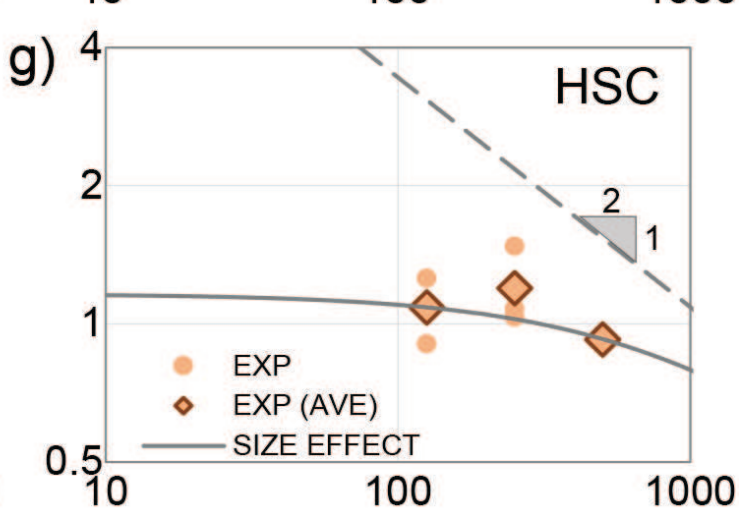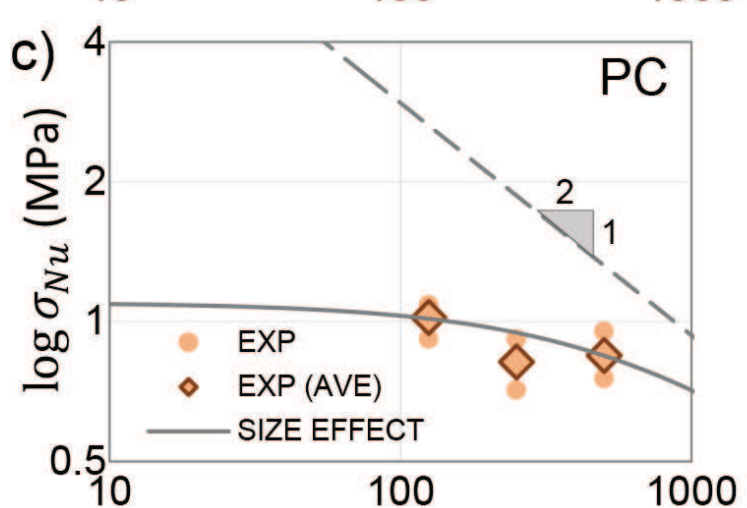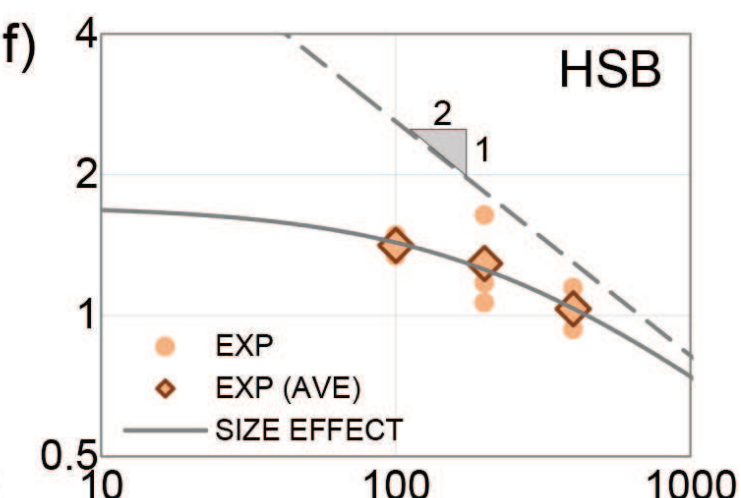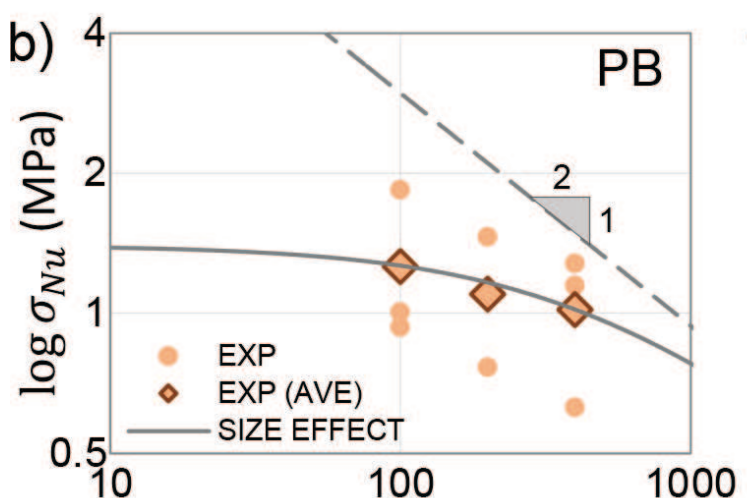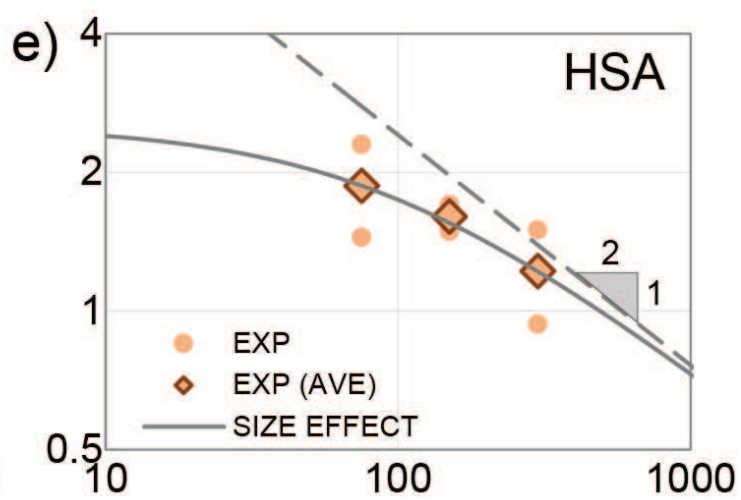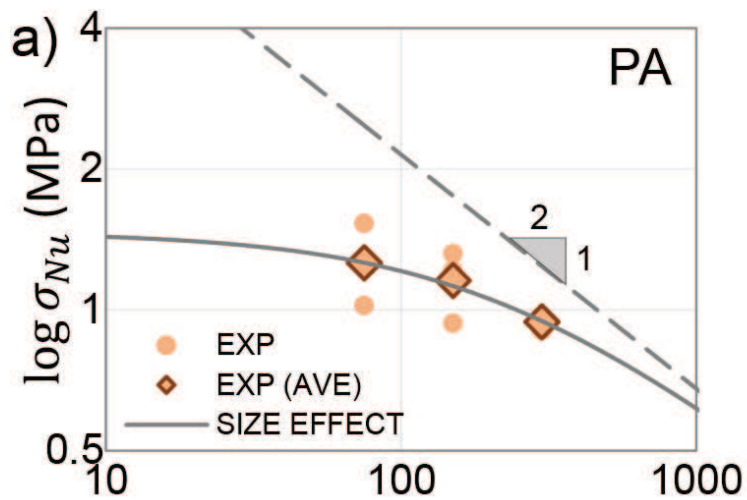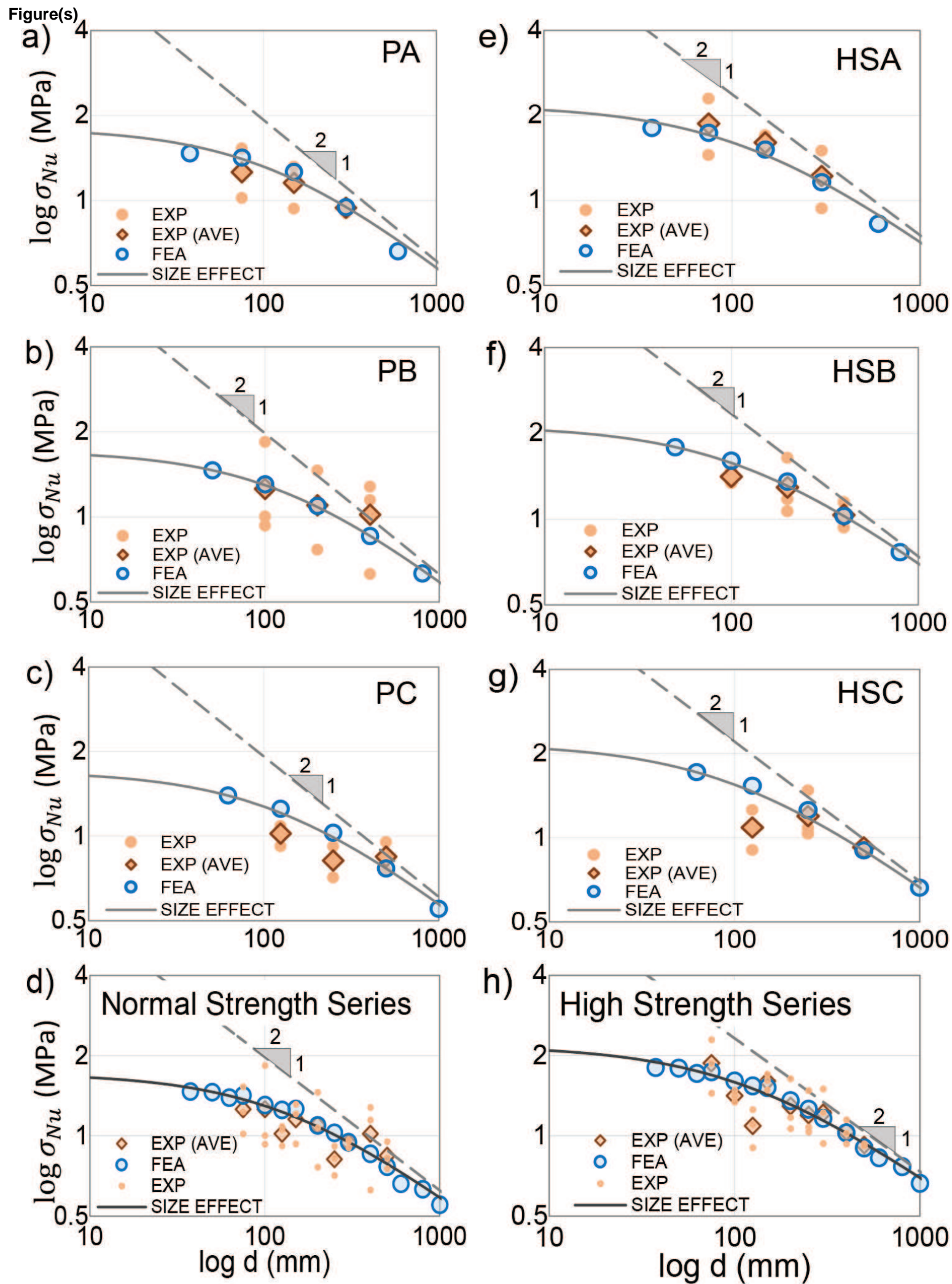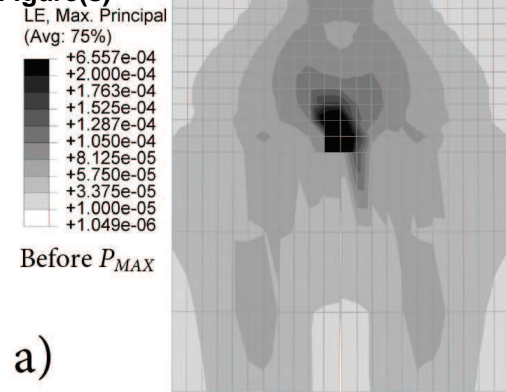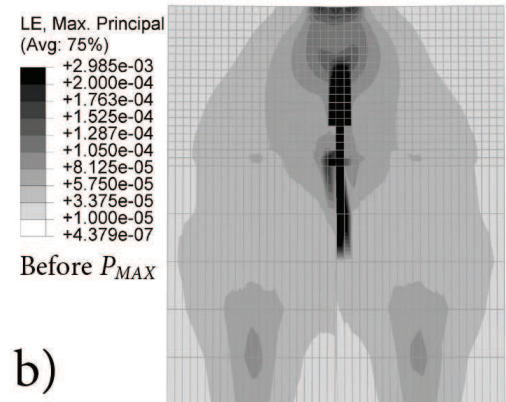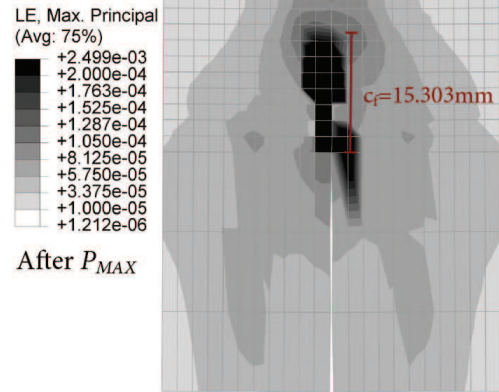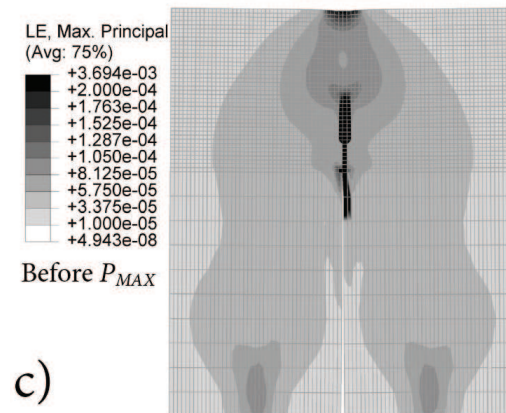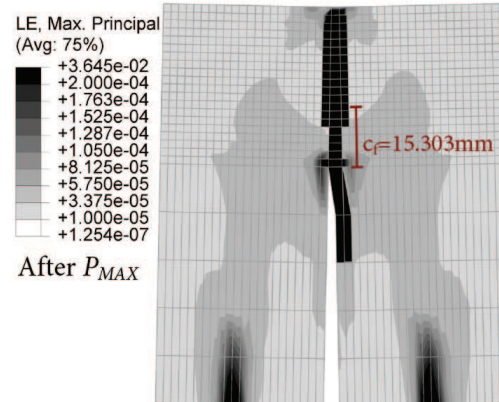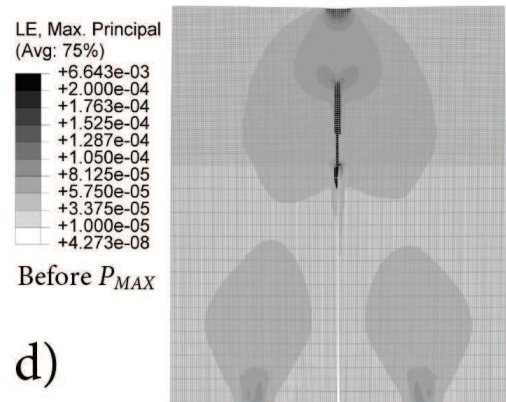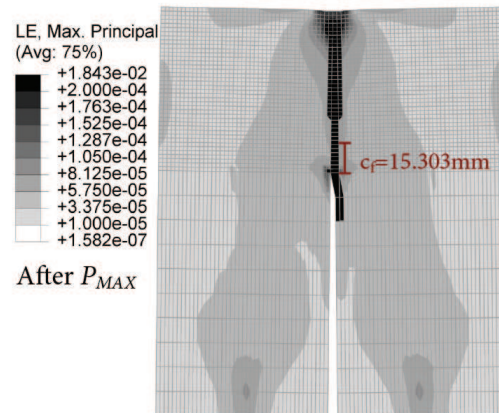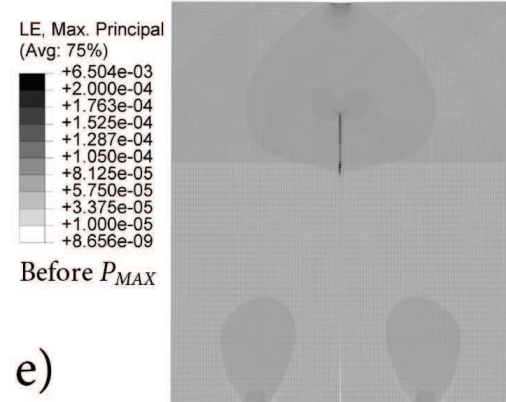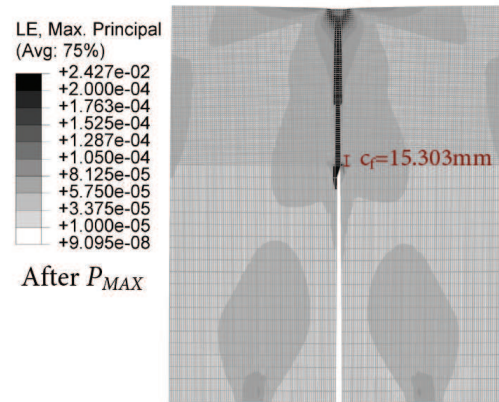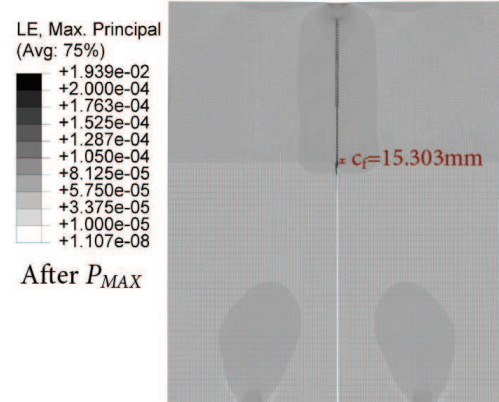
Before P_{MAX} — LE, Max. Principal (Avg: 75%): +6.965e-04, +2.000e-04, +1.763e-04, +1.525e-04, +1.287e-04, +1.050e-04, +8.125e-05, +5.750e-05, +3.375e-05, +1.000e-05, +1.041e-06
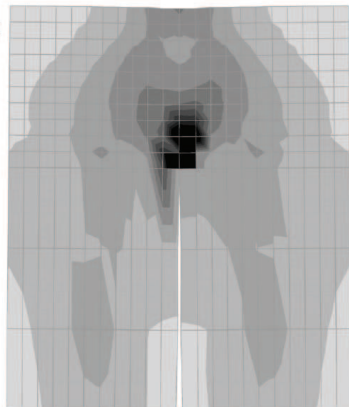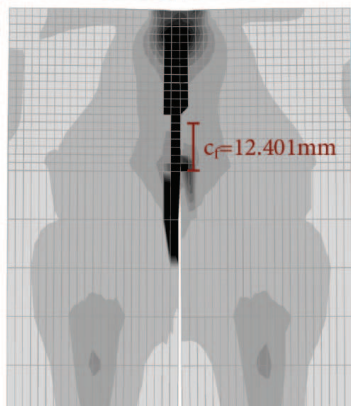
After P_{MAX} — LE, Max. Principal (Avg: 75%): +2.664e-03, +2.000e-04, +1.763e-04, +1.525e-04, +1.287e-04, +1.050e-04, +8.125e-05, +5.750e-05, +3.375e-05, +1.000e-05, +1.214e-06; c_f=12.401mm
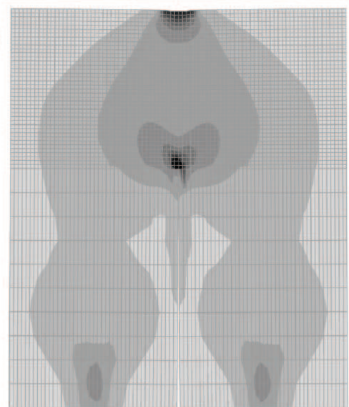
b)
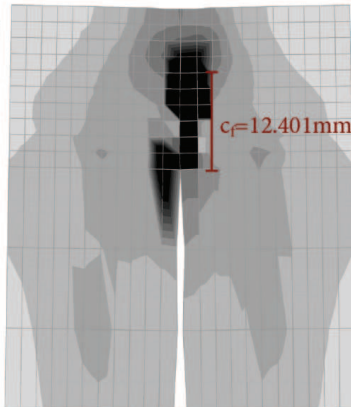
Before P_{MAX} — LE, Max. Principal (Avg: 75%): +4.456e-04, +2.000e-04, +1.763e-04, +1.525e-04, +1.287e-04, +1.050e-04, +8.125e-05, +5.750e-05, +3.375e-05, +1.000e-05, +4.564e-07
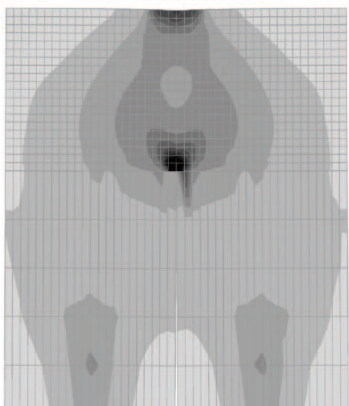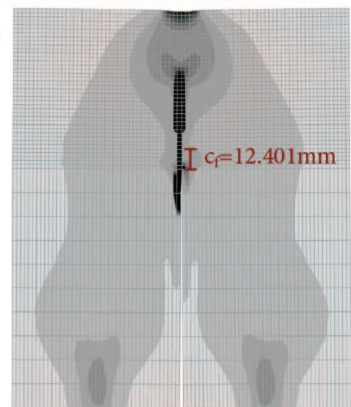
After P_{MAX} — LE, Max. Principal (Avg: 75%): +5.797e-03, +2.000e-04, +1.763e-04, +1.525e-04, +1.287e-04, +1.050e-04, +8.125e-05, +5.750e-05, +3.375e-05, +1.000e-05, +7.249e-07; c_f=12.401mm

c)

Before P_{MAX} — LE, Max. Principal (Avg: 75%): +5.924e-04, +2.000e-04, +1.763e-04, +1.525e-04, +1.287e-04, +1.050e-04, +8.125e-05, +5.750e-05, +3.375e-05, +1.000e-05, +1.110e-07

After P_{MAX} — LE, Max. Principal (Avg: 75%): +4.900e-03, +2.000e-04, +1.763e-04, +1.525e-04, +1.287e-04, +1.050e-04, +8.125e-05, +5.750e-05, +3.375e-05, +1.000e-05, +1.144e-07; c_f=12.401mm
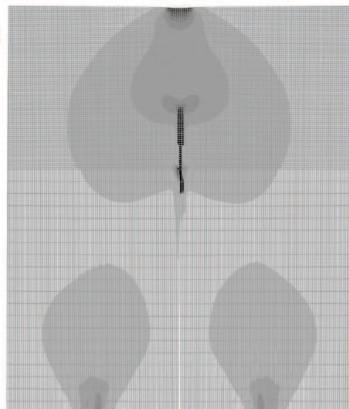
d)

Before P_{MAX} — LE, Max. Principal (Avg: 75%): +4.979e-03, +2.000e-04, +1.763e-04, +1.525e-04, +1.287e-04, +1.050e-04, +8.125e-05, +5.750e-05, +3.375e-05, +1.000e-05, +3.998e-08
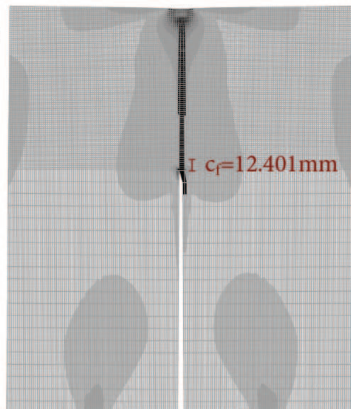
After P_{MAX} — LE, Max. Principal (Avg: 75%): +2.599e-02, +2.000e-04, +1.763e-04, +1.525e-04, +1.287e-04, +1.050e-04, +8.125e-05, +5.750e-05, +3.375e-05, +1.000e-05, +1.525e-07; c_f=12.401mm
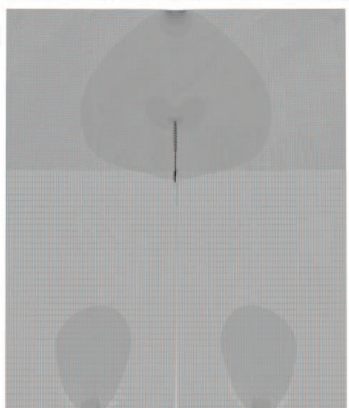
e)

Before P_{MAX} — LE, Max. Principal (Avg: 75%): +6.504e-03, +2.000e-04, +1.763e-04, +1.525e-04, +1.287e-04, +1.050e-04, +8.125e-05, +5.750e-05, +3.375e-05, +1.000e-05, +8.656e-09

After P_{MAX} — LE, Max. Principal (Avg: 75%): +1.939e-02, +2.000e-04, +1.763e-04, +1.525e-04, +1.287e-04, +1.050e-04, +8.125e-05, +5.750e-05, +3.375e-05, +1.000e-05, +1.107e-08; c_f=12.401mm